Radiochim. Acta **94**, 249–259 (2006) / **DOI** 10.1524/ract.2006.94.5.249
© by Oldenbourg Wissenschaftsverlag, München

Chemical speciation of heterogeneously reduced Pu in synthetic brines

By Mei Ding[1], James L. Conca[1], Christophe den Auwer[2], Rinat I. Gabitov[1,3,4], Nancy J. Hess[5], Patricia Paviet-Hartmann[1], Phillip D. Palmer[1], Vin LoPresti[1] and Steven D. Conradson[1,*]

[1] Los Alamos National Laboratory, Los Alamos NM 87545, USA
[2] CEA Marcoule, 30207 Bagnols sur Ceze Cedex France
[3] Rensselaer Polytechnic Institute, Troy, NY 12180, USA
[4] Institute of Experimental Mineralogy, Russia 142432
[5] Pacific Northwest National Laboratory, Richland, WA 99352, USA

(Received June 21, 2004; accepted in final form November 28, 2005)

Plutonium hydrous oxide / Reduction / Active barrier technology / XAFS / Chemical speciation / Local structure

Summary. X-ray absorption fine structure (XAFS) spectroscopy has been used to determine the speciation of Pu precipitates prepared by the heterogeneous reduction of Pu(VI) with Al and Fe in 5 M NaCl and an ERDA-6 brine, a simulant from the Waste Isolation Pilot Plant in Carlsbad, New Mexico. NaOCl was added to some of these solutions to determine its effect on Pu speciation. Analysis of the Pu L_{III} spectra showed that all solids consisted of $PuO_{2+x-y}(OH)_{2y}\cdot zH_2O$, compounds with characteristics identical to those prepared by hydrolysis and with Pu−O and Pu−Pu distances identical to those treated at elevated temperature. Additionally, reduction with Al gave compounds with different site distributions than reduction with Fe, and reduction with Al or the addition of NaOCl appeared to suppress the formation of oxo groups and their associated Pu(V) sites.

Introduction

The remediation of legacy transuranic (TRU)-contaminated waste from nuclear weapons production will ultimately cost tens to hundreds of billions of dollars. The magnitude of this problem is demonstrated by the fact that one of the two repositories in the U.S., the Waste Isolation Pilot Plant (WIPP) at Carlsbad, New Mexico, is dedicated solely to storage of this waste [1, 2]. Originally, these repositories were licensed under the assumption that geological constraints alone would prevent dissemination of radioisotopes for the duration specified in the license. However, given the realization – consistent with the tenets of Molecular Environmental Chemistry (MES) [3] – that speciation-specific behavior might well negate that assumption, there has recently been a shift toward consideration of other, shorter-term, designed chemical barrier processes. Active barrier technologies [4, 5] (even those deriving from the fortuitous Fe/Al composition of storage containers) represent one means for controlling and retarding the release of certain elements, including Pu. Pu is problematic in TRU waste because of its quantity, the 24,000 year half-life for its prevalent isotope, its range of valences within the repository environment that vary in their respective solubilities [6–11], the sensitivity of its chemistry to brine [12–27], its tendency to complex with other constituents of the WIPP milieu with concomitant change in solubility and sorption, its propensity for colloid formation [7, 12, 23, 28, 29], and its potential for producing redox-active radiolysis products [10, 13, 16, 27, 30–33]. In the case of WIPP, active barriers, including those provided by the metals in the container and possibly organic materials in the waste, raise the possibility of reducing higher-valence Pu to insoluble Pu(IV) species [23, 26, 27, 30, 34].

It has, however, been demonstrated that in aqueous NaCl solutions α particles from the radioactive decay of Pu produce oxidized chlorine species, including the hypochlorite ion, which readily oxidize Pu(IV) to Pu(VI) in concentrated NaCl solutions (> 3 M) and to Pu(V) in less-concentrated NaCl solutions (< 3 M) [13]. Pu(V) and Pu(VI) have thus been observed in a number of experiments conducted in brines [13, 16, 26, 31, 35].

Pu exhibits four (five under certain conditions) stable valences in aqueous systems, and it is possible to contrive conditions where all coexist, their relative stabilities highly influenced by potential ligands including chloride, nitrate, carbonate, *etc.* [6–8, 10]. Mobility, the inability to confine Pu to local waste repositories, is a measure of hazard of Pu. Pu valence is a key factor in assessing its solubility in groundwater, one of two critical factors determining Pu mobility; the second factor is its sorption on mobile colloids (NOM – natural organic material and silicates) that occur in groundwater. The importance of colloids has been clearly established; for example, Kersting *et al.* [36] have demonstrated colloidal transport of Pu-bearing clay and zeolite microparticles in the vadose zone at the Nevada Test Site, and McCarthy *et al.* [37] suggest that colloidal NOM enhances the transport of

*Author for correspondence (E-mail: conradson@lanl.gov).
Present address: MST-8 MS G755, Los Alamos National Laboratory, Los Alamos, NM 87 545, USA.

radionuclides in solutions that are undersaturated with respect to $Pu(OH)_4$ [28, 38].

Pu solubility in groundwater is mostly controlled by Pu(III), Pu(IV), and Pu(V) at the redox potential (Eh) and pH conditions corresponding to natural waters, where the dominant solid phase is $Pu(OH)_4$ [29]. The most important factor is the oxidation of the lower-valence species to the trans-dioxo configuration of the higher-valence ones, concomitant with a substantial increase in solubility. Instead of being spherically symmetric as it is in Pu(III) and (IV) complexes, the trans dioxo geometry is oblate, with the short multiply-bonded oxo groups on the poles and the equatorial ligands on the planes normal to the $PuO_2^{+/2+}$ axis. Transport models routinely assume that Pu(IV) (as PuO_2) is a thermodynamic well, so that, over time, the Pu valence will converge to it and that solubility of other Pu species is controlled by equilibrium with the pure PuO_2 phase. This can, however, be complicated by the chemistry specific to actinide-waste storage conditions. While Pu(VI) is usually reduced to the lower oxidation states under natural conditions, it is more stable at low pH, high Eh, and in solutions with a complex composition; therefore, its speciation and changes in that speciation can be significant with respect to the Pu(VI)-to-(IV) conversion [29]. For example, spectroscopic studies show that in 0.1 M $NaClO_4$, solid $Pu(VI)O_2CO_3$ is altered to solid $Pu(VI)O_2(OH)_2$ at pH = 4.5–9.0 and equilibrium atmospheric pressure of CO_2 [39], and hydroxide coordination can stabilize the higher valences. In the WIPP simulant brine ERDA-6, Pu(VI)-carbonate complexes are observed when carbonate is present, but, in their absence, Pu(VI) hydrolytic species predominate [18]. The $PuO_2(OH)_2$ complex has also been proposed to occur in solutions with total [Pu] $> 6 \times 10^{-5}$ M [38]. In acidic NaCl solutions and brines representative of the aquifers in salt formations, Pu(VI) forms PuO_2Cl^+ and $PuO_2Cl_2{}^0$ complexes [22]. The extreme conditions resulting from the saturated brine at WIPP therefore promote substitution reactions and the formation of complexes that are not typical of normal groundwater chemistry.

Still another potential complication to Pu(IV) chemistry is the complexity of PuO_2, which is assumed to be the final Pu(IV) convergence product of Pu species in the deposited waste. It has recently been shown that PuO_2 is more accurately described as $PuO_{2+x-y}(OH)_{2y} \cdot zH_2O$ and that the fully ordered structure is actually quite rare, with H_2O and its hydrolysis products incorporated as stable O^{2-} substitution products and, in addition, some fraction of the Pu present as Pu(V) with oxo groups [40–42]. In disagreement with the earlier suggestions that the Pu(V) (or VI) might retain mononuclear properties and be more easily leached from mixed-valence solids [43, 44], the experimental evidence indicates that it is actually stabilized within the PuO_2 lattice. Nevertheless, this variability suggests that different approaches to producing PuO_2 (such as heterogeneous reduction as compared with the more-normal hydrolysis procedure) and the presence of other components in the solution near saturation can perturb the structure, reactivity, and solubility of PuO_2-type solids.

One direct approach to rapidly immobilizing soluble Pu(V,VI) compounds is by precipitating them as Pu(IV) using reducing agents such as H_2O_2 [30, 32, 34, 45], metals [23], and organic complexants [33, 46]. Radiolysis also produces redox active species, such as the aforementioned hypochlorite, and these will be different in brines. Another α-radiolysis product, H_2O_2, reduces Pu(VI) not only in WIPP brines but also in HCl solutions [16, 25]. Finally, Pu in alkaline aqueous solution is also reduced directly by γ-radiolysis [13, 16, 33]. Although the yields are independent of pH, they are increased by organic compounds such as EDTA and formate [33]. This radiolytic reaction was reported to reduce the Pu(VI) to Pu(IV) hydroxide solid with a small admixture of Pu(VI), with unstable Pu(V) disproportionating to Pu(IV) and (VI) at pH < 9 [32, 33]. However, in the WIPP synthetic brine (ERDA-6B) at pH 9–12, the dominant oxidation state in solution after reduction with Fe powder was Pu(V) [23]. The proposed mechanism for the stability of the Pu(V) involved deactivation of the Fe because the formation of surface hydroxides in alkaline solutions passivated the Fe. In contrast, at higher pH, all the Pu(VI) precipitates as $PuO_2 \cdot xH_2O$ and $Pu(OH)_4$ from 0.01 M NaCl solution in the presence of Fe^0, with too little Pu remaining in solution to determine its valence [23].

These studies did not include direct identification of the Pu speciation in the precipitated solids. $Pu(OH)_3$, which is a possible species in the precipitate, is much more soluble than PuO_2-type species. Given that the PuO_2 system is much more complicated than was previously recognized, further characterization is required to accurately predict the expected behavior of Pu(IV) oxy-hydroxide solids [40–42, 47]. We have therefore undertaken the determination of the Pu speciation in the solid products of the reduction of Pu(VI) by Fe and Al in WIPP synthetic brines, to which NaOCl was added in some cases to determine its influence on Pu reduction. This characterization employed X-ray Absorption Fine Structure (XAFS) spectroscopy measurements at the Pu L_{III} edge. XAFS has been recognized as one of the most incisive methods in the MES armory because of its high degree of accuracy in directly determining average speciation and its low potential for interference from the matrix, thus obviating the need for extensive sample preparation that may introduce artifacts [3, 47, 48]. These measurements show that the heterogeneous reduction converts > 99% of the original Pu(VI) in the solution into $PuO_{2+x-y}(OH)_{2y} \cdot zH_2O$ compounds, identical to those prepared by hydrolysis and with the same Pu−O and Pu−Pu distances found in such compounds prepared at elevated temperature. However, some differences in the Pu speciation, which correlate with the method of preparation, are also observed.

Materials and methods

Preparation of XAFS samples

0.005 M $^{239}Pu(VI)$ in pH = 2 hydrochloric acid was used as the initial tracer solution. Two solutions were used: 5 M NaCl (pH = 7.50) and the WIPP simulant brine, ERDA-6 (pH = 8.40), which represents a NaCl-dominated brine collected from the Castile formation situated at depth below the WIPP. Details regarding preparation of synthetic brines and chloride solution used in this study can be found in the

papers by Lu *et al.* [24, 25]. Iron and Al powders used in the experiments, purity 99+%, were obtained from Aldrich. NaOH, HCl, NaOCl, and all other chemicals used were analytical grade. Two types of brine solutions were prepared. NaCl solutions were made by adding 1 ml of 0.005 M Pu(VI) stock solution to 3.6 ml of 5 M NaCl and the pH was adjusted to 7.8. The other solutions were made by adding the same quantity of Pu(VI) stock solution to 2 ml of WIPP Castile formation simulant "ERDA" brine containing the following salts dissolved in H_2O to a total volume of 1000 ml: 23.74 g Na_2SO_4, 1.13 g NaBr, 23.70 g $Na_2B_4O_7 \cdot 10H_2O$, 261.64 g NaCl, 1.34 g $NaHCO_3$, 7.32 g KCl, 3.86 g $MgCl_2 \cdot 6H_2O$, 1.76 g $CaCl_2 \cdot 2H_2O$, plus 1 ml of 0.01 M HCl; pH was adjusted to 7.8. Final concentrations were as follows: 93,400 ppm Na^+, 3000 ppm K^+, 482 ppm Mg^{2+}, 91 ppm Ca^{2+}, 585 ppm B, 644 ppm Br^-, 140,000 ppm Cl^-, and 13,700 ppm SO_4^{2-}. 0.4 ml and 1.0 ml of 0.01 M NaOH were added, respectively, to the 5 M NaCl and ERDA solutions lacking added NaOCl. 1 ml of 0.01 M NaOCl was added to the others. A control solution of the same amount of the Pu(VI) stock solution added to 4 ml H_2O was also prepared. 500 mg of Fe powder (< 10 μm) was added to the five different types of solutions. 500 mg of Al powder (< 20 μm) was added to the two ERDA solutions – with and without NaOCl. After four weeks of gentle shaking, the solids were separated by centrifugation and decantation. The final pH was 7.45–7.72. Liquid scintillation measurements on the liquid phase showed essentially quantitative ($> 99\%$) removal of the Pu in all samples. The recovered solids served as samples for XAFS analysis.

Sample preparation and data collection

The PuO_2 and Pu(VI) aquo standards have been reported elsewhere [49]. The samples were ground in a mortar and pestle with BN. The resulting powders were poured into slots in an aluminum holder and held in place by a Kapton window in the front and a polyethylene cap in back. Samples were mounted in a liquid N_2-cooled cryostat to minimize the thermal contribution to the Debye–Waller factors. XAFS measurements were performed at beamline 11-2 of the Stanford Synchrotron Radiation Laboratory, under dedicated synchrotron x-ray production conditions (3.0 GeV e^-, 80 mA). Si(220) crystals were used to monochromate the beam, with a Pt-coated flat mirror tilted to have a cut-off energy of 22–25 keV used to eliminate harmonics in the fully tuned mode. Spectra were obtained in the fluorescence mode by monitoring the L_{β_1} emission line using 24–30 elements of a multi-element Ge detector array and digital amplifiers. The integration window was set to include the full L_{β_1} fluorescence peak to maximize the total count rate for the Pu. The energies were calibrated by using the transmitted beam to measure the absorbance of a Zr foil placed between the second and a third ion chamber simultaneously within the scans of the samples. The first inflection point of this spectrum was defined as 17,999.35 eV. Insofar as the highest sample absorbance over the edge was 0.16 and the internal count rates for this sample ranged from 65–96 000 maximum, distortions of the white line amplitude from self-absorption or dead-time correction errors are negligible.

Data analysis

Second-order polynomials were fit through both the pre-edge region below the absorption edge and the post-edge region above it to mimic the smooth backgrounds. The spectrum was offset to set the value of the extrapolated pre-edge polynomial to zero at E_0, defined as 18,075 eV. The spectra were normalized by scaling them to set the value of the extrapolated post-edge polynomial to unity at $E_0 = 18{,}075$ eV (Fig. 1a). Multiple scans were averaged after interpolating the data of the individual scans to match one set of energies. The extended fine structure was separated from the spectra by approximating the smooth, atomic background with a polynomial spline, with the knot positions adjusted to minimize the area of the modulus of the Fourier transform of the k^3-weighted EXAFS below $R = 1.0$ Å. After this procedure, E_0 was redefined as 18,067 eV. Fourier transforms were always calculated after the application of a sine window function to the EXAFS. Metrical parameters were obtained from the EXAFS weighted by k^3 *via* nonlinear, least-squares k-space curve fits using the standard, harmonic EXAFS equation summed over shells and amplitudes and phases obtained from code FEFF7 [50]. The phases of the data in k and the moduli and real parts of the transforms in R were compared with those of the fits for each shell to

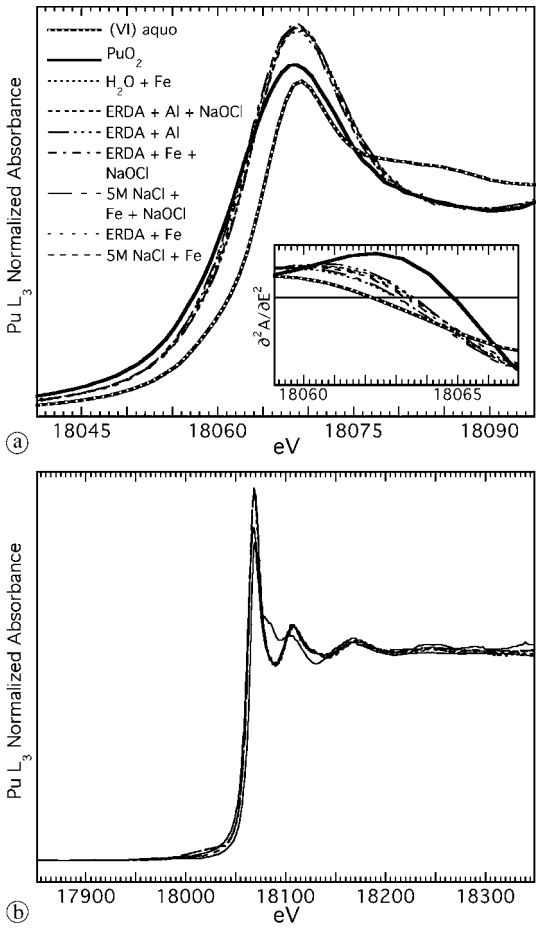


Fig. 1. (a) Pu L_{III} X-ray Near Edge Absorption Spectra of indicated samples. Normalized absorbance and second derivatives through the inflection point (inset). (b) Normalized Pu L_{III} X-ray Absorption Spectra of indicated samples to show pre-edge and post-edge absorbance and close grouping of spectra over entire energy range.

evaluate the level of confidence in these assignments. Errors were obtained by calculating the least squares error to the fit with and without the wave from a particular shell to determine its overall improvement in the quality of the fit. The floating parameters were then varied until the quality of the fit was worse by 10% of this contribution.

A total of nine shells were fit, one Pu, seven O with Pu−O < 3.6 Å, and an O shell at 4.5 Å (with a total number of O atoms with Pu−O < 3.6 Å set to be 6 < total < 10). Additionally, two shells (three for ERDA + Al + NaOCl sample) had separations below the resolution limit of the spectra used for the main shell and were fit with an *R*-average of approximately 2.33 Å to allow the O distribution to be anharmonic. All other shells have resolved separations and should reflect actual shells when the number of atoms is significant. *R* and *N* were allowed to float for every shell, Debye–Waller factors were allowed to float for shells with $2.1 < R < 2.4$ but were constrained to be equal for these two (three for ERDA + Al + NaOCl sample) shells. The Debye–Waller factor for all other O shells with Pu−O < 3.6 Å was fixed at 0.045 Å, a value determined through trial and error to yield best curve fits with a reasonable total number of atoms; although not necessarily physically realistic (σ should increase with Pu−O distance), it is useful in explaining the complexity of the Pu environment with respect to its O nearest neighbors. The Debye–Waller factor for Pu was allowed to float, and for the 4.5 Å O shell, was fixed at 0.070. Errors were calculated for all sigmas, even when they were fixed. The number of floating parameters totaled 20 with two constraints. Hence the fits encompass 18 degrees of freedom, well under the maximum of 27 allowed [51].

Results and discussion

X-ray absorption near edge structure (XANES)

As previously discussed, XANES provides primary speciation information on the Pu [49, 52], XANES spectra making it possible to distinguish the different valences of Pu present in experimental compounds. As simple absorbance spectroscopy, XANES adheres to Beer's law, thereby allowing the Pu valence of the final products of Pu(VI) reduction to be identified in the experimental samples despite the presence of multiple valences. Unreduced Pu(VI) that coprecipitated with Pu(IV) in the experimental samples would shift the edge to higher energy, diminish the amplitude of the main peak, and increase the absorbance beyond it relative to the spectrum of PuO_2 [47, 53]. Given that none of these effects are observed (Fig. 1a) and that the absorption peak in the precipitates is actually substantially larger than in the spectrum of ordered PuO_2 (Table 1), the overall shape and position of the Pu peak strongly suggests the absence of Pu(VI) in these heterogeneously reduced samples to within the 5%–10% sensitivity limits of the method. The virtual identity of all spectra (Fig. 1a) demonstrates that this is true for all experimental samples. The pre- and post-edge spectra illustrate the close similarity of spectra from all samples over the entire energy range (Fig. 1b), indicating that normalization was not responsible for the creation of artifacts.

Further interpretation of the XANES is complicated because of various competing structure-spectrum correlations and the complexity of the $PuO_{2+x-y}(OH)_{2y}\cdot zH_2O$ system [49]. The excess O in PuO_{2+x}-type compounds has been shown to consist of oxo groups associated with Pu(V) [40–42], for which the only stable configuration known is the trans-dioxo PuO_2^+ moiety. Oxo groups are found not only as the result of oxidation of PuO_2 with H_2O at elevated temperature but also upon hydrolytic precipitation of Pu(IV) from aqueous solution. The absorption edges of Pu(IV) and (V) species exhibit considerable overlap, making it difficult to identify signatures of Pu(V) in a mixture with Pu(IV), by contrast to the relatively simple distinction between Pu(IV) and Pu(VI). Insofar as there are several structural features that influence spectra at the edge, there is no single alteration of the XANES that can be assigned to the Pu(V) species. Its contribution to the XANES is so small that the spectra are only minimally or negligibly modified in response to changes in the number of oxo groups determined by EXAFS analysis across the range found for this set of compounds. Considering the small fraction of Pu(V) present and that the spectral changes associated with Pu(V) are minimal (energy) and ambiguous (IV overlap), it is impossible to correlate spectral changes with this fraction of Pu(V).

The XANES of the seven experimental solids, herein, are not only indistinguishable from one another (Fig. 1), but also display main peak amplitudes and edge energies higher than those of PuO_2 and are essentially identical within experimental error to the spectra of solids made by precipitation from aqueous solution [41, 42]. The similarity of these spectra indicate that the experimental solids are chemically indistinguishable from those generated by pH controlled hydrolysis of Pu(IV) solutions. In our already cited investigations of the $PuO_{2+x-y}(OH)_{2y}\cdot zH_2O$ system [41, 42, 49], the

Table 1. XANES parameters: Edge inflection point of ordered reference $PuO_2 = 18{,}062.3$ eV based on first inflection point of Zr metal = 17,999.35 eV.

Sample	Edge energy	ΔeV PuO_2	Peak energy	Peak height
PuO_2[a]	18062.3 ± 0.3	reference	18068.6 ± 0.3	1.55
Fe: 5 M NaCl	18063.4	1.1	18069.1	1.70
Fe: ERDA	18063.1	0.8	18068.7	1.72
Fe: 5 M NaCl NaOCl	18063.3	1.0	18068.6	1.73
Fe: ERDA NaOCl	18063.5	1.2	18069.0	1.70
Al: 5 M ERDA	18063.6	1.3	18069.0	1.71
Al: 5 M ERDA NaOCl	18063.5	1.2	18068.7	1.71
Fe: H_2O	18063.0	0.7	18068.8	1.69

a: Uncertainty for PuO_2 from two independent samples that gave very similar EXAFS; errors for other spectra are most likely close to this value.

spectra of samples that display structural disorder relative to crystallographic PuO_2 can be divided into those prepared in the solid state at elevated temperature because their absorption peaks and edge energies are always lower than those of PuO_2 and those prepared by precipitation from aqueous solution at ambient temperature that exhibit higher peak amplitudes and edge energies. The correlated shift in edge energy is at least partly attributable to a narrowing of the peak that occurs when its amplitude is higher. The amplitude of the white line and edge energy of ordered $PuO_{2.00}$ therefore fall in the middle. If the height of this peak was simply associated with ordering (from, for example, the annealing that occurs at elevated temperature), then that of $PuO_{2.00}$ would be expected to show one extreme of amplitude. Its occurrence between the two types of samples is difficult to explain. However, we have observed that the white line amplitude of Pt L_{III} edges is affected by stereochemistry. This suggests the possibility of a similar origin herein, an effect of the three-dimensional arrangement of the various types of O-based ligands to the Pu, which would have negligible effects on the one-dimensional distribution probed by the EXAFS of these materials. Whatever the mechanism, the significant result is that reductive and hydrolytic precipitation of $PuO_{2+x-y}(OH)_{2y}\cdot zH_2O$ produce materials that are identical in this respect.

Comparisons of spectra, $\chi(k)$ and $\chi(R)$

The $\chi(k)$ spectra of PuO_2-type compounds (Figs. 2–9) are distinguished by the following features: large-amplitude envelopes of the O waves dominate at lower k followed by a transition region where the high-frequency Pu−Pu wave is first evidenced at $k = 7.5\,\text{Å}^{-1}$; then the large-amplitude Pu−Pu is wave the major component at higher k. In this study, the phases of all sample spectra display the following features: three periods up to $k = 7\,\text{Å}^{-1}$ from the low-frequency, nearest-neighbor Pu−O wave; a small peak just below $k = 8\,\text{Å}^{-1}$; and five more periods through $k = 12.5\,\text{Å}^{-1}$. Spectra with this general pattern are characteristic of all PuO_2-type compounds, with the differences among them being the extent of the damping, as detailed in Figs. 3 through 9.

In regular crystalline materials with well-separated shells of atoms, the modulus of the Fourier transform of the EXAFS, $\chi(R)$, is related to the radial distribution function of the absorbing element. The modulus only represents half the information, the real or imaginary component of the transform providing the remainder and subsuming the phase information in curve fits. When these conditions are met and interference is minimized, the peaks represent shells of

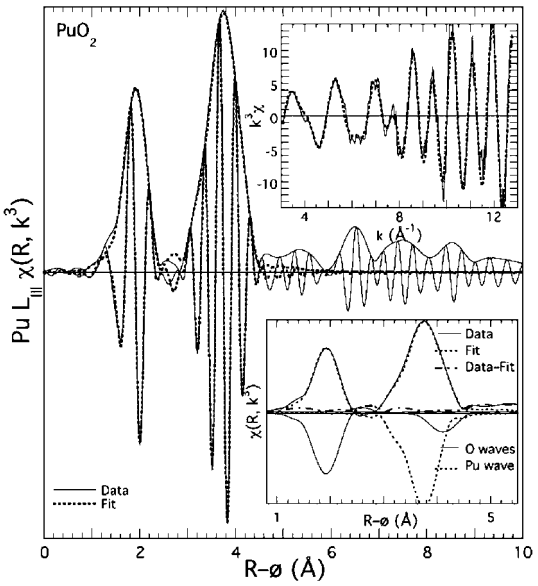


Fig. 2. Fourier transform, $\chi(R)$, of spectrum of ordered PuO_2. The solid is the modulus and real component of the data, the dotted is of the fit. The upper inset shows the data and fit in k. The lower inset shows the moduli of the data, fit, and difference, and the contributions of the individual shells.

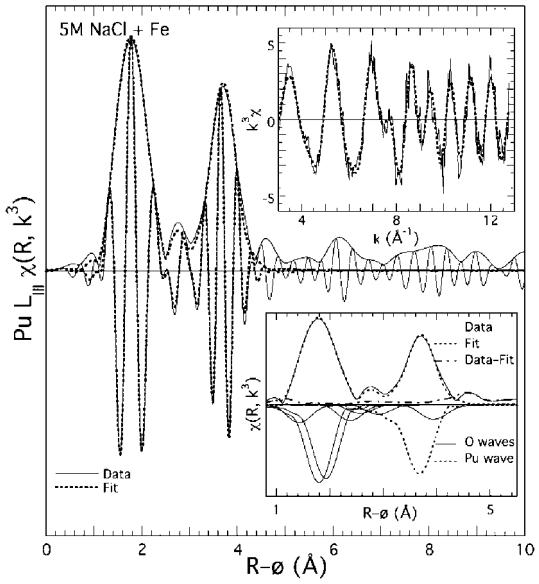


Fig. 3. Fourier transform, $\chi(R)$, of spectrum of 5 M NaCl + Fe samples. The solid is the modulus and real component of the data, the dotted is of the fit, the upper inset shows the data and fit in k. The lower inset shows the moduli of the data, fit, and difference, and the contributions of the individual shells.

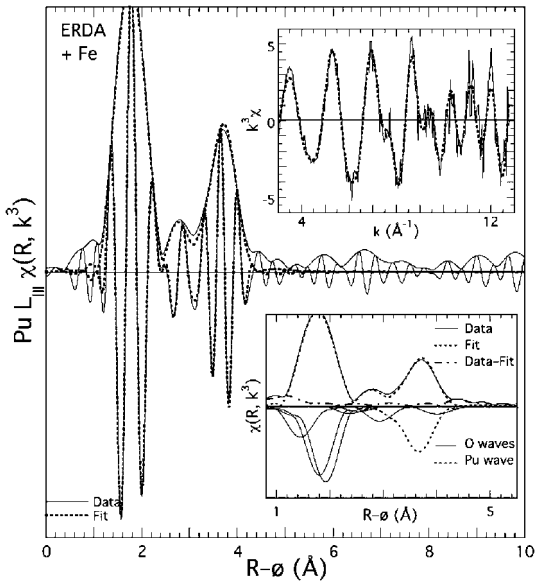


Fig. 4. Fourier transform, $\chi(R)$, of spectrum from ERDA + Fe sample, as in Fig. 3. The scale of the main figure is identical to that of Fig. 3.

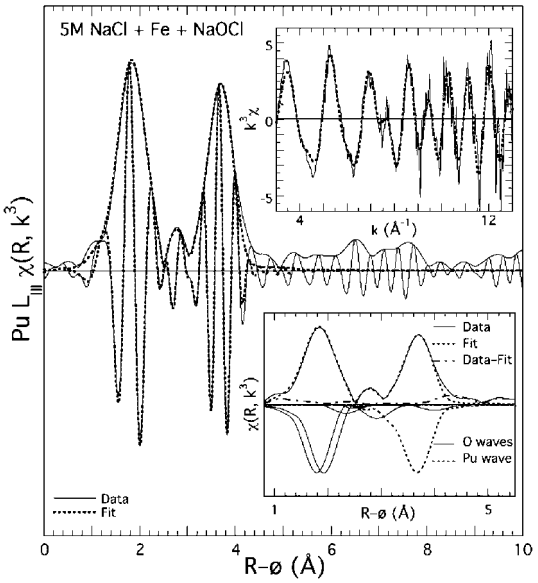


Fig. 5. Fourier transform, $\chi(R)$, of spectrum from 5 M NaCl + Fe + NaOCl sample, as in Fig. 3. The scale of the main figure is identical to that of Fig. 3.

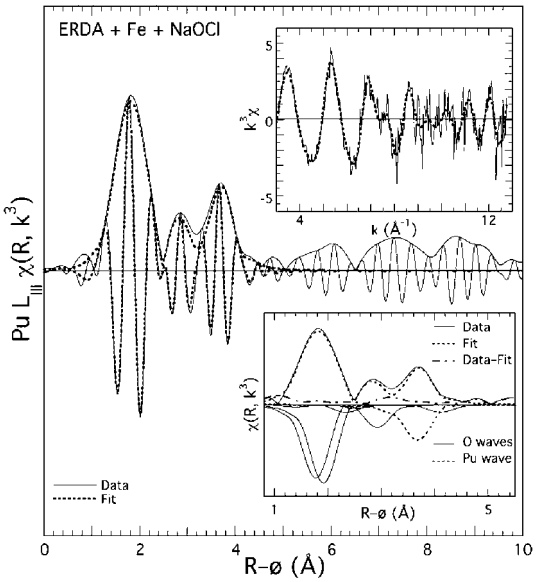


Fig. 6. Fourier transform, $\chi(R)$, of spectrum from ERDA + Fe + NaOCl sample, as in Fig. 3. The scale of the main figure is identical to that of Fig. 3.

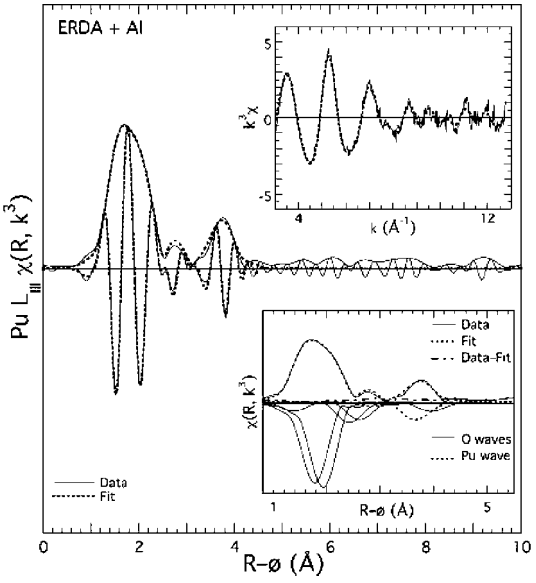


Fig. 7. Fourier transform, $\chi(R)$, of spectrum from ERDA + Al sample, as in Fig. 3. The scale of the main figure is identical to that of Fig. 3.

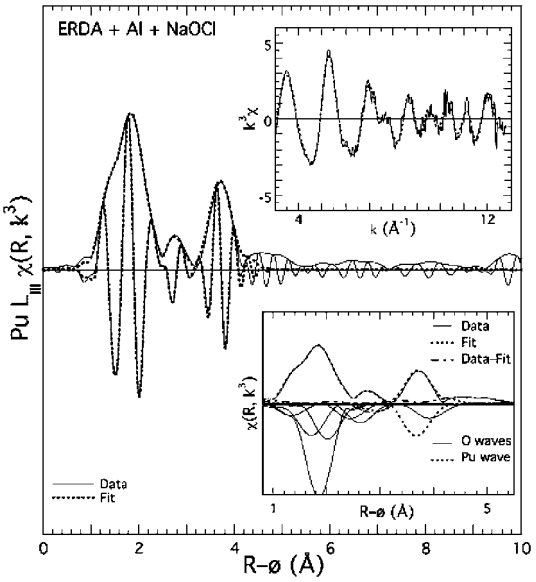


Fig. 8. Fourier transform, $\chi(R)$, of spectrum from ERDA + Al + NaOCl sample, as in Fig. 3. The scale of the main figure is identical to that of Fig. 3.

neighbor atoms, although their positions in $\chi(R)$ are lowered by the phase shift. This is seen (Fig. 2) in the $\chi(R)$ modulus for PuO_2 where the first peak at $R = 1.9$ Å corresponds to the O shell at 2.33 Å, the second at $R = 3.7$ Å to the Pu shell at 3.83 Å, and the extended order continues to give additional peaks out to high R. This spectral structure pattern, with its implied similarity in local structure, occurs in the $\chi(R)$ of all seven experimental samples. These two prominent peaks demonstrate that all seven are members of the $PuO_2/PuO_{2+x-y}(OH)_{2y}\cdot zH_2O$ class of compounds. However, to second order, there are many differences among the spectra – most notably amplitude reduction in these two peaks, especially the Pu – and the disappearance of those peaks at longer distances. Additionally, the O peak is broad and often exhibits shoulders and asymmetry, and the region from $R = 2.6$–3.0 Å displays a variable feature with a larger relative amplitude. For most of the samples, the minimum in the modulus just past the O peak near $R = 1.4$ Å is shifted to higher R than that of PuO_2, showing that the O peak has more of a tail. The small feature between the O and Pu peaks at $R = 2.4$–2.6 Å (which must be mostly Fourier ripple in the spectrum of ordered PuO_2) is large relative to the main peaks and variable in these samples so that the beginning of the Pu peak is delayed to much higher R. In the spectrum of PuO_2, this region lacks structural features between the crystallographic O and Pu shells (Fig. 2), these small peaks in the experimental samples implying that there may be O shells with Pu−O distances between 2.5 and 3.6 Å. This situation is similar to that in $PuO_{2+x-y}(OH)_{2y}\cdot zH_2O$ prepared by oxidation at elevated temperature and hydrolysis of Pu(IV) [40−42].

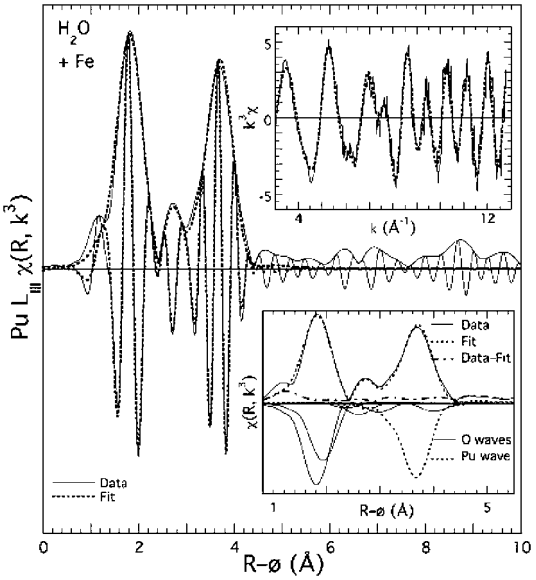


Fig. 9. Fourier transform, $\chi(R)$, of spectrum from $Fe + H_2O$ control sample, as in Fig. 3. The scale of the main figure is identical to that of Fig. 3.

The Pu peaks in the spectra from Pu reduced by Al and the ERDA + Fe + NaOCl sample are substantially lower than the Pu peaks in the other four experimental samples, consistent with either a reduced number of Pu atoms and/or a more disordered Pu−Pu distribution. The samples reduced with Al also show a less symmetric and more structured O peak. Closer inspection of the region between the O and Pu peaks may also show whether the details of the preparation method affect the local structure. By tracking the real component, it is evident that all samples show local maxima around $R = 2.25$, 2.55, 2.9, and 3.4 Å (Figs. 3–9). However, the moduli of the spectra from the Pu reduced with Al (Figs. 7 and 8) are lower in amplitude and flatter than the others from $2.5 < R < 2.9$ Å and the real component above 2.9 Å does not display the large dip at around $R = 3.1$–3.2 Å. The spectra from the Fe-reduced samples do not show any gross deviations, with the exception of the lower position of the $R = 3.05$ Å local minimum for the ERDA + Fe + NaOCl sample.

Curve-fit results, Pu−O shells with Pu−O > 2.1 Å

Good fits were obtained for all spectra, although some show larger residuals than others. These fits utilized five O shells with Pu−O distances between 2.2 and 3.4 Å, in addition to the Pu and 4.47 Å O shells and the 1.85 Å O shell (when present) (Table 2). The exception was the ERDA + Al + NaOCl sample, which required six O shells in a different pattern. Correlation between interfering waves can result in runaway amplitudes, the sum of a combination of similar waves remaining small even as the individual waves become very large; as a consequence, fine-tuning of the composite wave is necessary to better fit the data. For the reported

Table 2. Curve-fitting results.

Sample	O shells, Pu−O < 3.6 Å								Pu		O at 4.5 Å	
Crystal structure			2.3368						3.81612		4.47424	
PuO_2-ordered Sample 1	*R*		2.34 ±0.02						3.83 ±0.01		4.53 ±0.02	
	N		7.4 ±2.1						10.0 ±2.4		23.0 ±7.2	
	σ		0.076±0.013						0.067±0.007		0.087±0.012	
PuO_2-ordered Sample 2			2.33 ±0.02						3.82 ±0.01		4.53 ±0.02	
			7.2 ±2.1						8.9 ±2.2		14.9 ±4.7	
			0.077±0.013						0.056±0.007		0.077±0.012	
5 M NaCl + Fe	1.86 ±0.02	2.24 ±0.02	2.37 ±0.023		2.81 ±0.02	3.00 ±0.02	3.34 ±0.02		3.80 ±0.01		4.43 ±0.02	
	0.4 ±0.1	4.0 ±1.1	4.2 ±1.0		0.7 ±0.3	0.5 ±0.1	0.6 ±0.1		6.0 ±1.9		4.9 ±2.6	
	0.045±0.010	0.079±0.013	0.079±0.013		0.045±0.011	0.045±0.005	0.045±0.005		0.074±0.010		0.070±0.012	
ERDA + Fe	1.88 ±0.02	2.25 ±0.02	2.36 ±0.02		2.80 ±0.02	2.97	3.36 ±0.02		3.79 ±0.01		4.50 ±0.02	
	0.7 ±0.2	3.7 ±0.9	4.5 ±1.1		0.4 ±0.2	0.3	1.1 ±0.4		2.7 ±0.09		3.1 ±1.5	
	0.045±0.012	0.074±0.013	0.074±0.013		0.045±0.008	0.045	0.045±0.018		0.048±0.011		0.070±0.013	
5 M NaCl + Fe +NaOCl		2.24 ±0.02	2.37 ±0.02		2.77 ±0.02	3.04 ±0.02	3.35 ±0.02		3.80 ±0.01		4.49 ±0.02	
	0	4.0 ±1.2	4.5 ±1.3		0.4 ±0.1	0.1 ±0.1	0.9 ±0.2		3.4 ±2.0		1.9 ±2.9	
		0.087±0.015	0.087±0.015		0.045±0.006	0.045±0.006	0.045±0.025		0.045±0.009		0.070±0.011	
ERDA + Fe +NaOCl	1.83 ±0.01	2.23 ±0.02	2.37 ±0.02		2.77 ±0.02	2.97 ±0.02	3.35 ±0.02		3.80 ±0.01		4.60 ±0.02	
	0.1 ±0.0	3.7 ±1.1	4.5 ±1.2		0.3 ±0.2	0.2 ±0.2	1.3 ±0.4		2.3 ±0.6		2.4 ±1.1	
	0.045±0.004	0.087±0.015	0.087±0.015		0.045±0.008	0.045±0.007	0.045±0.018		0.067±0.011		0.070±0.014	
ERDA + Al	1.81 ±0.12	2.22 ±0.02	2.38 ±0.02		2.86 ±0.02	3.05 ±0.02		3.59	3.77±0.02		4.45 ±0.02	
	0.2 ±0.1	3.6 ±0.9	4.3 ±1.0		0.8 ±0.2	0.8 ±0.2		0.2	6.0 ±0.8		2.6 ±1.6	
	0.045±0.010	0.080±0.011	0.080±0.011		0.045±0.015	0.045±0.016		0.045	0.13±0.011		0.070±0.013	
ERDA + Al +NaOCl	1.77 ±0.02	2.16 ±0.02	2.30 ±0.01	2.45 ±0.01	2.87 ±0.02	3.06 ±0.02	3.29 ±0.02		3.79±0.02		4.42 ±0.02	
	0.2 ±0.1	1.5 ±0.4	4.9 ±1.0	1.2 ±0.4	0.7 ±0.3	1.0 ±0.3	0.6 ±0.1		8.3 ±1.6		5.0 ±1.9	
	0.045±0.016	0.078±0.012	0.078±0.010	0.045±0.013	0.045±0.016	0.045±0.006	0.045±0.006		0.12±0.009		0.070±0.012	
H_2O + Fe		2.26 ±0.02	2.38 ±0.02		2.79 ±0.02	3.04 ±0.02	3.41 ±0.02		3.80 ±0.01		4.50 ±0.02	
		4.7 ±1.3	3.7 ±1.0		0.2 ±0.1	0.6 ±0.2	0.7 ±0.2		3.8 ±1.0		3.0 ±1.0	
		0.084±0.014	0.084±0.015		0.045±0.011	0.045±0.014	0.045±0.013		0.046±0.012		0.070±0.015	

R = Pu−O/Pu distance; *N* = number of atoms in shell; σ = Debye–Waller factor.

fits, the constraints on the total number of O atoms and the Debye–Waller factors maintained all O-shell amplitudes at levels not greatly exceeding spectral amplitudes. The main O peak is fit by two shells of comparable number; but since the 0.12 Å to 0.16 Å separation falls within the 0.13 Å resolution limit, they possibly indicate an anharmonic distribution rather than two distinct Pu−O shell distances. A projected beat just beyond the range of the data is a common effect that effectively damps the amplitude with more freedom in its shape than a Debye–Waller factor acting on a single wave. A beat past the limit of the data suppresses the amplitude while avoiding the phase shift and subsequent rise in amplitude that define the beat, differentiating it from damping caused by disorder. The differences among the various samples in the overall amplitude of this peak were handled in the fit by the Debye–Waller factor, which was constrained to equality for the two overlapping shells.

The mid-range region was fit by O shells near 2.8, 3.0, and 3.4 Å. The shortest of these is necessary to fit the extended tail on the main O peak and the combination of the other two gives the modulus peak around $R = 2.8$ Å that occurs for all samples but not in the ordered PuO_2 spectrum. Parameter correlation is apparent in that smaller Debye–Waller factors for these shells give lower numbers of atoms, which are coupled to larger numbers of atoms and Debye–Waller factors for the primary O shell. Similarly, smaller separations in distance and more equal numbers of atoms for the first two of these shells diminish the overall amplitude of the fit and conversely, larger separation and, more disparate numbers of atoms increase amplitude. The wide variation and large deviation from the crystallographic values for the O shell with Pu−O = 4.47 Å demonstrates that the disorder has reduced its contribution to the spectra below that at which it can be positively identified.

The spectrum of the ERDA + Al + NaOCl sample (Fig. 8) – with the high shoulder on the low-R side of the main O peak – required a different basic model for a good fit. Instead of two, three overlapping O shells at 2.16, 2.30, and 2.45 Å were required to fit the primary O contribution. The 0.15 Å separation is equivalent to a phase shift of π so that these Pu−O waves at the ends will act to reduce the amplitude of the central wave. This effect is seen in the transform modulus of the contributions of the individual waves relative to the data and provides a means for fitting the shoulder and overall width with a fixed number of nearest neighbors. The amplitudes of the next O shells are also somewhat high relative to the data, a result similar to that for the ERDA + Al spectrum but not for the spectra of the Fe-reduced samples. Since the spectra of the Al-reduced and Fe-reduced samples were found to differ in this region, it is hoped that the curve fits can provide additional details regarding the differences. A plot of Pu radial distribution functions, Fig. 10, a graphical presentation of curve-fit results that provides a more incisive means for examining these data.

The amplitudes of the O shells at approximately 2.8 and 3.05 Å in both Al-reduced samples are somewhat high relative to the data, an effect not seen in Fe-reduced samples, and the 2.8 Å O shell also shifts to higher distance in both Al spectra. This will cause its wave to interfere more with the 3.05 Å wave and accounts for the increased amplitude of both shells in curve fits. The ERDA + Al spectrum did not include an O shell near 3.3 Å, but instead, had a small one near 3.6 Å overlapping the Pu shell. As noted, the primary O shell also exhibits more structure in the Al-reduced samples. Hopefully, additional curve fits can elucidate the differences between samples reduced by the two metals, which currently in their approximation of the distribution give more O weight to the Al-reduced samples – relative to the Fe-reduced ones – at distances below 3.1 Å and less weight above 3.1 Å.

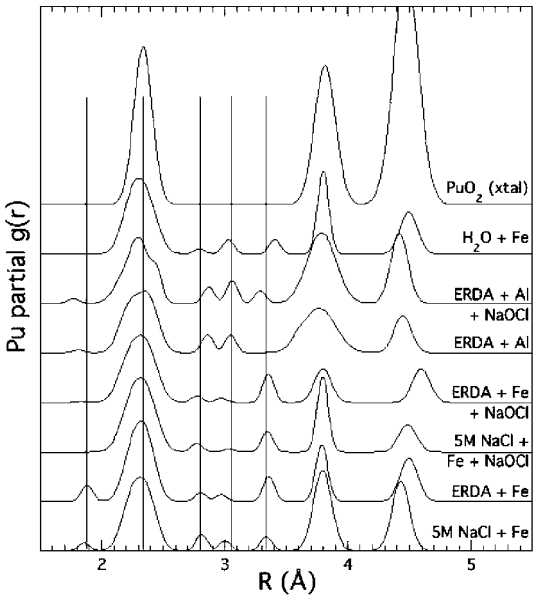


Fig. 10. Pu partial radial distribution functions from indicated samples, calculated directly from the curve-fit results. The width is given by the Debye–Waller factor and the number of atoms for a shell or overlapping set of shells is equal to the area under the peaks. Vertical lines are placed at positions where O shells are found in other materials prepared by hydrolysis and reaction at elevated temperature. All peaks are O shells with the exception of that near 3.8 Å, which is the Pu.

Curve-fit results, Pu shell

All of the Pu−Pu distances are within experimental error of the crystallographic distance except for the ERDA + Al, which also displayed the lowest Pu-peak amplitude among all spectra. Anharmonicity in the distribution, which is known to yield shorter distances in curve fits, might explain this contracted distance. Correlation between the number of atoms and Debye–Waller factor makes it difficult to identify the Pu-shell amplitude behavior solely from curve fits. The number of atoms is defined by the amplitude at low (actually 0) k before the wave is damped by disorder. The small amplitude of the Pu wave in combination with the large O-wave amplitude and noise and background residuals makes it problematic to accurately determine this distance. The unreliable measure of the number of Pu atoms greatly exacerbates the difficulty in separating the number and the Debye–Waller factor and fosters such situations in which the spectra with the smallest Pu peaks give the largest numbers in the curve fits. The Al-reduced samples, which display the smallest Pu peaks in the spectra, give the largest numbers of atoms in the fit because these spectra are evidently best fit with very large Debye–Waller factors. Adjusting the Debye–Waller factors could rectify this. There is, however,

no justification for preferring one value to another. To set them at the average from the other five samples would ignore the fact that the low amplitudes most likely are at least partly the result of increased disorder.

The problem of cation disorder in AnO_{2+x} and its effect on EXAFS has been evaluated in more detail in recent work on the UO_{2+x} system [54]. The optimal solution to this problem is to examine the spectra rather than automatically assuming the validity of the curve-fit results. The spectra indicate that the Al-reduced samples have a lower Pu amplitude than the Fe-reduced ones that most likely originates in disorder involving some combination of a decrease in the number of Pu neighbors and a broadening, possibly anharmonic, of the Pu−Pu distribution. An examination of the prior step in the curve-fit process reveals that although the spline knots were comparable for all of the spectra (by design), the somewhat different $\chi(k)$ behavior of the Al-reduced samples did yield splines with distinctly different curvatures. This background contributes to the high amplitude at low k that results in high numbers of atoms and Debye–Waller factors in the curve fits and is at least partly responsible for these discrepancies. The possibility that there are Al atoms in the precipitate that produce the wave with this shape was checked by doing fits with a Pu−Al wave. These gave significantly worse results than Pu−Pu waves, indicating that the precipitates are predominantly Pu-oxide with little or no substitution or inclusion of other elements near this position.

Oxo shell, Pu–O < 2 Å

A final O shell representing an oxo-type ligand exists at a Pu−O distance of 1.8–1.9 Å. This shell only occurs in the more soluble Pu(V,VI) complexes and is also a signature for the effectiveness of the reduction, or reoxidation by OCl^-. Although curve fits for several of the samples can include this shell, it is significant only in samples reduced by Fe in the absence of NaOCl. The Pu−O distances for these spectra are also consistent with the relatively long ones found in PuO_{2+x}, [40–42] whereas those samples whose spectra indicate only very small amounts of oxo atoms also have unusually short distances. These results were corroborated by direct inspection of the original $\chi(R)$ spectra over the region where the oxo group makes its contribution (Fig. 11). Recently, another group found that the inclusion of oxo groups potentially improved the quality of fits of EXAFS of Pu(IV) colloids [55]. The spectral behavior was attributed to a two-electron excitation that produced a second edge, rather than to the actual presence of an oxo group. Nonetheless, the identification of a spectral feature directly associated with the oxo-type shell and correlated with its discovery by curve fits demonstrates that the EXAFS wave is not an artifact of the fitting procedure, but rather corroborates the assignment to this structural feature.

The imaginary parts of the spectra of the two Fe-reduced/no NaOCl samples display a high relative maximum near $R = 1.36$ Å followed by a deep minimum near $R = 1.56$ Å. The $H_2O + Fe$, $ERDA + Al + NaOCl$, and $5\,M\ NaCl + Fe + NaOCl$ spectra either exhibit these features at significantly different positions or show different ones. These differences are manifest after the contributions of overlapping shells have been subtracted, leaving the

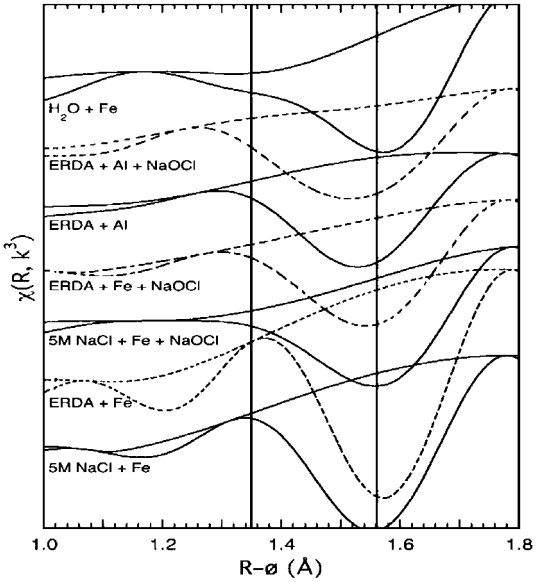


Fig. 11. Expansion of low R region of Fourier transform, $\chi(R)$, of indicated samples where the oxo group present in PuO_{2+x} makes its contribution, as in Fig. 2. Both moduli and real parts are shown.

contributions from oxo groups as the only structural component in the spectra. The Fe-reduced/no-NaOCl spectra exhibit a maximum in the modulus near $R = 1.4$ Å, and the real component displays a maximum just below that point and a local minimum near $R = 1.54$ Å. These features in the $ERDA + Al$ and $ERDA + Fe + NaOCl$ spectra are much smaller and either different or shifted. Hence, they will not be well fit by a Pu−O wave, and the amplitude for such a wave will be lower than the background residuals and other errors in the data, and therefore, insignificant. This spectral examination confirms the curve-fit results and demonstrates that all except for the two Fe/no-NaOCl samples are inconsistent with the presence of oxo groups.

Concluding remarks

To reiterate the most important finding: the heterogeneous reduction of Pu(VI) in brines (and H_2O) gives Pu species identical to the $PuO_{2+x-y}(OH)_{2y}\cdot zH_2O$ compounds prepared by other methods. The salient characteristics of these species are a multisite Pu−O distribution, including a disordered, broad, primary O shell; additional O shells with Pu−O distances around 2.8, 3.05, and 3.4 Å; a single-site but (highly) disordered Pu distribution that may include a reduction in the number of Pu neighbors and, in some cases, oxo groups that are believed to be associated with Pu(V) sites. The conservation of the average Pu sublattice means a retention of the original diffraction pattern of PuO_2. The range of Pu−O bonds is indicative of coordination to OH^- and possibly H_2O, as well as displacements of these O atoms to specific locations that give the longer Pu−O bonds. The Pu disorder may include vacancies and substitution by H^+. Despite their high concentrations, there is no sign that any of the brine components, neither anionic nor cationic, are incorporated into the PuO_2 host at the $\sim 10\%$ sensitivity level of the method. This is true for the reducing agents as well. Furthermore, the correspondence of the speciation is closer to those

PuO_2-type compounds made by hydrolysis in aqueous solution than to those exposed to elevated temperature. Beyond this, the following significant patterns differentiating these samples are observed:

- Although all of the samples are disordered relative to PuO_2, those reduced by Fe have more symmetric O shells and Pu shells that give larger modulus peaks.
- NaOCl suppresses the formation of oxo-Pu(V) species in the solids.
- Reduction by Al gives more highly structured primary O distributions while suppressing Pu(V)-oxo species, the more distant mid-range O shells, and the amplitude of the Pu peak in the modulus.
- Removal of the brine so that the reaction occurs in buffered H_2O solution has no significant effect on the product of the reduction by Fe.

Insofar there is no sign that Al or Fe ions resulting from this reduction are incorporated into these products, it is reasonable to surmise that the differences in the Pu speciation associated with the different reductants originate in the kinetics of their formation, disorder being typically associated with increased formation rate. It should be noted, however, that precipitate formation involves multiple steps, both on the surface of the metal phase and in solution. The difference in speciation and structure may be significant in terms of transport if associated with colloid formation. Should it be possible to control or even to influence the size and structure of particles of precipitated $PuO_{2+x-y}(OH)_{2y}\cdot zH_2O$ by as simple a means as adjusting the reagents used in their preparation, then these results have important implications for Pu storage and remediation. High ionic strength is usually associated with colloid aggregation, but in these reactions it had only minimal or negligible effects on speciation. The type or even presence of the brine apparently does not significantly affect the speciation of the Pu solids, at least when reduced by Fe.

Finally, based on a homogeneous model for PuO_{2+x}, it has been postulated that the higher valence Pu(V) would be more soluble and therefore more easily leached out of the host compound, increasing the environmental hazard of these materials [44]. In contrast, local structure measurements, including these, have found that the oxidized Pu species appear to form because they are stabilized by the lattice and are therefore not susceptible to such leaching. Where it occurred, the fraction of Pu(V) in the solid was much greater than the amount of Pu remaining in solution that was also well under the solubility limit. This departure from the results expected from the chemistry of the homogenous or mononuclear species is also corroborated by the observation that the addition of OCl^- was associated with products that were less rather than more oxidized. This paradox is more understandable in the context of reaction anomalies originating in collective behavior among the Pu sites and other structural components of the solids that give them unusual reactivity than it is by novel mechanisms involving isolated Pu complexes.

Acknowledgment. Modeling and background studies associated with this work were supported by DOE NNSA/DP and OBES Division of Chemical Sciences under Contract W-7405. All experimental measurements were performed at the Stanford Synchrotron Radiation Laboratory, a national user facility operated by Stanford University on behalf of the U.S. Department of Energy, Office of Basic Energy Sciences. Health Physics support at SSRL was provided by the Los Alamos National Laboratory section of the Seaborg Institute for Transactinium Science.

References

1. *The Waste Isolation Pilot Plant: a potential solution for the disposal of transuranic waste*. National Academy Press, Washington, D.C. (1996) p. 169.
2. *The Waste Isolation Pilot Plant*. U.S. DOE Carlsbad Field Office (2004).
3. DOE sponsored workshop on molecular environmental science: speciation, reactivity and mobility of environmental contaminants, and an assessment of research opportunities and the need for synchrotron radiation facilities. Airlie, Virginia (1995).
4. Zoumis, T., Calmano, W. Forstner, U.: Acta Hydrochim. Hydrobiol. **28**, 212 (2000).
5. Jacobs, P. H. Waite, T. D.: Chemosphere **54**, 313 (2004).
6. Cleveland, J. M.: *The Chemistry of Plutonium*. Am. Nucl. Soc., Illinois (1979) p. 653.
7. Choppin, G. R.: Radiochim. Acta **32**, 43 (1983).
8. Katz, J. J., Morss, L. R., Seaborg, G. T.: *The Chemistry of the actinide elements*. Chapman and Hall, London, (1986).
9. Choppin, G. R.: Radiochim. Acta **43**, 82 (1988).
10. Choppin, G. R., Bond, H. A., Hromadka, P. M.: J. Radioanal. Nucl. Chem. **219**, 203 (1997).
11. Cooper, N. G., Buican, I. G., Schecker, J. A. (eds.): Los Alamos Science vol. 26: Challenges in Plutonium Science. Los Alamos National Laboratory, Los Alamos, New Mexico (2000) p. 500.
12. Newton, T. W., Baker, F. B.: J. Phys. Chem. **61**, 934 (1957).
13. Buppelmann, K., Kim, J. I., Lierse, C.: Radiochim. Acta **44**/**45**, 65 (1988).
14. Choppin, G. R.: Mar. Chem. **28**, 19 (1989).
15. Felmy, A. R., Rai, D., Mason, M. J.: Radiochim. Acta **55**, 177 (1991).
16. Pashalidis, I., Kim, J. I., Lierse, C., Sullivan, J. C.: Radiochim. Acta **60**, 99 (1993).
17. Reed, D. T., Okajima, S., Richmann, M. K.: Radiochim. Acta **66**, 95 (1994).
18. Reed, D. T., Okajima, S., Richmann, M. K.: Radiochim. Acta **66**, 105 (1994).
19. Rao, L., Rai, D., Felmy, A. R.: Radiochim. Acta **72**, 151 (1996).
20. Langmuir, D.: In: *Aqueous Environmental Geochemistry*. Langmuir, D. (ed.) Prentice-Hall, Inc., New Jersey (1997) p. 529.
21. Rai, D., Felmy, A. R., Sterner, S. M., Moore, D. A., Mason, M. J., Novak, C. F.: Radiochim. Acta **79**, 239 (1997).
22. Runde, W., Reilly, S. D., Neu, M. P.: Geochim. Cosmochim. Acta **63**, 3443 (1999).
23. Xia, Y., Rao, L., Rai, D., Felmy, A. R.: J. Radioanal. Nucl. Chem. **250**, 27 (2001).
24. Lu, N., Conca, J. L., Hartmann, T., Paviet-Hartmann, P., Parker, G. R., Martinez, B. A., Strietelmeier, E. A.: Los Alamos National Laboratory Report, LA-UR-02-3665 (Los Alamos National Laboratory, Los Alamos, New Mexico (2002)) p. 33.
25. Lu, N., Paviet-Hartmann, P., Palmer, P. D., Hartmann, T., Conca, J. L., Strietelmeier, E. A. Parker, G. R.: Los Alamos National Laboratory Report, LA-UR-02-4165 (Los Alamos National Laboratory, Los Alamos, (2002)) p. 46.
26. Villareal, R., in CBFO/EPA Working Meeting (2002).
27. Reed, D. T., Aase, S. B., Kropf, A. J., Conca, J. L.: AIP Conf. Proc. **673**, 372 (2003).
28. Knopp, R., Neck, V., Kim, J. I.: Radiochim. Acta **86**, 101 (1999).
29. Runde, W., Conradson, S. D., Efurd, D. W., Lu, N. P., VanPelt, C. E., Tait, C. D.: Appl. Geochem. **17**, 837 (2002).
30. Oak, M. S., Ghadse, D. R., Sagar, V. K., Patil, S. K.: Radiochem. Radioanal. Lett. **59**, 139 (1983).
31. Garnov, A. Y., Yusov, A. B., Shilov, V. P., Krot, N. N.: Radiochem. **40**, 17 (1998).
32. Shilov, V. P., Budantseva, N. A.: Radiochem. **40**, 568 (1998).
33. Pikaev, A. K., Gogolev, A. V., Shilov, V. P.: Radiat. Phys. Chem. **56**, 483 (1999).

34. Marsh, S. F., Martinez, E. A., Day, R. S., Nixon, A. E.: Los Alamos National Laboratory Report, LA-12554A (Los Alamos National Laboratory, Los Alamos (1993)) p. 8.
35. Garnov, A. Y., Yusov, A. B., Shilov, V. P., Krot, N. N.: Radiochem. **40**, 219 (1998).
36. Kersting, A. B., Efurd, D. W., Finnegan, D. L., Rokop, D. J., Smith, D. K., Thompson, J. L.: Nature **397**, 56 (1999).
37. McCarthy, J. F., Williams, T. M., Liang, L. Y., Jardine, P. M., Jolley, L. W., Taylor, D. L., Palumbo, A. V., Cooper, L. W.: Environ. Sci. Technol. **27**, 667 (1993).
38. Okajima, S., Reed, D. T.: Radiochim. Acta **60**, 173 (1993).
39. Pashalidis, I., Kim, J. I., Ashida, T., Grenthe, I.: Radiochim. Acta **68**, 99 (1995).
40. Conradson, S. D., Begg, B. D., Clark, D. L., Den Auwer, C., Espinosa-Faller, F. J., Gordon, P. L., Hess, N. J., Hess, R., Keogh, D. W., Morales, L. A., Neu, M. P., Runde, W., Tait, C. D., Veirs, D. K. Villella, P. M.: Inorg. Chem. **42**, 3715 (2003).
41. Conradson, S. D., Begg, B. D., Clark, D. L., Den Auwer, C., Ding, M., Dorhout, P. K., Espinosa-Faller, F. J., Gordon, P. L., Haire, R. G., Hess, N. J., Hess, R. F., Keogh, D. W., Morales, L. A., Neu, M. P., Paviet-Hartmann, P., Runde, W., Tait, C. D., Veirs, D. K., Villella, P. M.: J. Am. Chem. Soc. **126**, 13 443 (2004).
42. Conradson, S. D., Begg, B. D., Clark, D. L., den Auwer, C., Ding, M., Dorhout, P. K., Espinosa-Faller, F. J., Gordon, P. L., Haire, R. G., Hess, R. F., Keogh, D. W., Lander, G. H., Manara, D., Morales, L. A., Neu, M. P., Paviet-Hartmann, P., Rebizant, J., Rondinella, V. V., Runde, W., Tait, C. D., Veirs, D. K., Villella, P. M., Wastin, F.: J. Solid State Chem. **178**, 521 (2005).
43. Stakebake, J. L., Larson, D. T., Haschke, J. M.: J. Alloys Compd. **202**, 251 (1993).
44. Haschke, J. M., Allen, T. H., Morales, L. A.: Science **287**, 285 (2000).
45. Morgenstern, A. Choppin, G. R.: Radiochim. Acta **86**, 1 (1999).
46. Reed, D. T., Wygmans, D. G., Aase, S. B., Banaszak, J. E.: Radiochim. Acta **82**, 109 (1998).
47. Conradson, S. D.: Appl. Spectrosc. **52**, 252A (1998).
48. Teo, B. K.: EXAFS: Basic principles and data analysis. Springer-Verlag, New York (1986) p. 349
49. Conradson, S. D., Abney, K. D., Begg, B. D., Brady, E. D., Clark, D. L., den Auwer, C., Ding, M., Dorhout, P. K., Espinosa-Faller, F. J., Gordon, P. L., Haire, R. G., Hess, N. J., Hess, R. F., Keogh, D. W., Lander, G. H., Lupinetti, A. J., Morales, L. A., Neu, M. P., Palmer, P. D., Paviet-Hartmann, P., Reilly, S. D., Runde, W. H., Tait, C. D., Veirs, D. K., Wastin, F.: Inorg. Chem. **43**, 116 (2004).
50. Ankudinov, A. L., Rehr, J. J.: Phys. Rev. B **56**, R1712 (1997).
51. Stern, E. A.: Phys. Rev. B **48**, 9825 (1993).
52. Ankudinov, A. L., Conradson, S. D., de Leon, J. M., Rehr, J. J.: Phys. Rev. B **57**, 7518 (1998).
53. Morris, D. E., Allen, P. G., Berg, J. M., Chisholm-Brause, C. J., Conradson, S. D., Donohoe, R. J., Hess, N. J., Musgrave, J. A., Tait, C. D.: Environ. Sci. Technol. **30**, 2322 (1996).
54. Conradson, S. D., Manara, D., Wastin, F., Clark, D. L., Lander, G. H., Morales, L. A., Rebizant, J., Rondinella, V. V.: Inorg. Chem. **43**, 6922 (2004).
55. Rothe, J., Walther, C., Denecke, M. A., Fanghanel, T.: Inorg. Chem. **43**, 4708 (2004).